HATSOPOULOS MICROFLUIDS LABORATORY

Department of Mechanical Engineering, Massachusetts Institute of Technology

Slippage and Migration in Taylor-Couette Flow of a Model for Dilute Wormlike Micellar Solutions

Louis F. Rossi, Gareth McKinley, L. Pamela Cook

June, 2005
HML Report Number 05-P-06

HML@MIT
http://web.mit.edu/fluids

Slippage and Migration in Taylor-Couette Flow of a Model for Dilute Wormlike Micellar Solutions

Louis F. Rossi, [a] Gareth McKinley, [b] L. Pamela Cook [a]

[a] *Department of Mathematical Sciences*
University of Delaware
Newark, DE 19716
USA

[b] *Department of Mechanical Engineering*
Massachusetts Institute of Technology
Cambridge, MA 02139
USA

Abstract

In this paper we explore a model, most appropriate for dilute or semi-dilute worm-like micellar solutions, in an axisymmetric circular Taylor-Couette geometry. This study is a natural continuation of earlier work on rectilinear shear flows. The model, based on a bead-spring microstructure with nonaffine motion, reproduces the pronounced plateau in the stress strain-rate flow curve as observed in laboratory measurements of steady shearing flows. We also carry out a linear stability analysis of the computed steady state solutions. The results show shear-banding in the form of sharp changes in velocity gradients, spatial variations in number density, and in alignment or stretching of the micelles. The velocity profiles obtained in numerical solutions show strong qualitative agreement with those of laboratory experiments.

Key words: Mathematical modeling, inhomogeneous fluids, dumbbell models with slippage, wormlike micellar solutions, Taylor-Couette flow.

1 Introduction

Worm-like micellar solutions are of special interest due to their extensive commercial applications and due to their unusual behavior under different flow conditions [RH91]. Worm-like micelles are very long cylindrical structures composed of amphiphilic surfactant molecules which self-assemble in

solution. These structures are flexible and can entangle and behave much like polymers in solution, however they can also spontaneously break and reform on different time scales. Thus, they have earned the name "living polymers" [Cat87]. Of special interest is the behavior of dilute and semi-dilute worm-like micellar solutions under shearing flow. Two characteristics observed in experiments of dilute micellar solutions have been the source of considerable experimental and theoretical investigation. First, solutions can become turbid with increasing shear rate as the result of a shear-induced phase separation (SIPS) [LNWP,LNK$^+$]. Second and of more interest to the present study, the flow curve of steady shear stress versus shear rate presents a distinct plateau [Ber97,BRP94]. Flow visualization of micellar solutions in this plateau region shows the formation of shear-bands [LFHY05,SCMM03,LNWP,LNK$^+$,HL04,WHC03]. A number of models have been proposed to explain these phenomena. In this paper, we apply a bead-spring model including a non-affine slippage term developed in [CR04] to describe worm-like micellar solutions in circular Taylor-Couette flows.

One of the suggested mechanisms for shear banding is that of a constitutive instability. That theory suggests that an underlying non-monotone relationship between stress and strain-rate, in shearing flow, is responsible for the existence of shear banded solutions. In this description, specific shear bands consist of identical stress states on different branches of the flow curve corresponding to different strain rates. A number of studies of this behavior have focused on Johnson-Segalman-like models, that is models in which the convected derivative is a Gordon-Schowalter derivative. In early papers, studies were carried out investigating possible mechanisms for a unique choice of shear banding possibilities [EYB96,GB97,NP97]. In order to have a model which selects unique states, higher order derivative (diffusive) terms were needed [Olm99]. In conjunction with this diffusive terms were added to the constitutive relation [LOB00,Olm99,ORL00,RO00]. More recently two fluid effects and couplings between the flow and the microstructure, for example coupling between the stress and the mean micellar length, have been investigated [FO03a,FO03b,FO04]. Some of the most recent studies are especially relevant to experimental studies which suggest that a steady state banding pattern is not achievable, and instead oscillatory banding patterns appear [WFF98,FO04]. In particular the recent NMR study by Lopez-Gonzalez et al. [LGHCP04] demonstrated a clear connection between shear-band instability and flow-microstructure coupling. In those studies mentioned above in which the Gordon-Schowalter derivative is used in the modeling, it is used phenomenologically, rather than being systematically derived from a fundamental principle or microscopic model.

In an earlier paper [CR04], a new model was presented for semi-dilute solutions of wormlike micellar solutions in which the non-affine motion was tracked consistently in the modeling process. Recent studies of wormlike mi-

cellar solutions have demonstrated that there can be a sequence of rheological transitions as the concentration of surfactant and counter-ion are progressively increased; from the dilute to the semi-dilute/entangled and ultimately to the concentrated/entangled regime. The present model is most appropriate for the semi-dilute/entangled regime in which the deformation of individual wormlike micelles (rather than network segments) is followed. The effects of chain overlap and entanglement and the continuous breaking and reforming of the wormlike micelles in the semi-dilute regime are modeled by the non-affine deformation of the microstructure. The model was derived using kinetic theory assuming that the viscoelastic characteristics of the semi-dilute solution properties could be lumped into a bead-spring mechanism. The model self-consistently incorporates "slippage/tumbling" as well as the spatial extension of the bead-spring. This work is a generalization of the Bhave, Armstrong, Brown model for dilute polymers [BAB91], as presented and corrected by Beris and Mavrantzas [BM94], to nonaffine motions. In particular, the model equations form a system of partial differential equations in which the number density, velocity gradients, velocity and stress are coupled. The inclusion of "slippage/tumbling" in the model yields the Gordon-Schowalter convected derivative in the stress equation and the incorporation of spatial extension couples the stress equation with an evolution equation for the local number density of micellar chains. The latter equation is dependent on shear rate variations, stress variations, and the slippage parameter. In the previous paper, the predictions of the model were examined in rectilinear steady state shearing flow. It was shown, computationally, as anticipated [Olm99] that the addition of the extra terms, especially the diffusive terms, removed the indeterminacy in the steady state shear banded state. Calculation of the steady-state shear stress versus shear-rate curve for this model shows that the shear stress first increases with shear rate, then plateaus, and only rises again at much higher shear rates. Thus, the viscosity as a function of shear rate first decreases slowly (slight shear thinning) as the shear-rate increases, then drops quickly proportional to $\dot{\gamma}^{-1}$ and then, at much higher shear rates, levels off to its asymptotic solvent limit.

The inclusion of slippage/tumbling effects incorporates a nonaffine motion into the model [Lar88]. This nonaffine motion is consistent with breakage and re-formation of the wormlike micelles under an imposed shearing deformation. The measure of the nonaffine motion is $\xi = 1 - a$. When $a = 1$, $\xi = 0$, the motion is affine. As a decreases from 1, the motion becomes more strongly nonaffine. Shear banding behavior and the concurrent stress plateau can only occur if the underlying flow curve is nonmonotone, that is if $\xi \neq 0$, or more precisely if $|a| < 1$ and $\beta < n_0 a^2/8$ where n_0 is the core number density. (See Section 3.)

The generic trends observed in the flow curve discussed above are typical of results of experimental measurements of wormlike micellar solutions which ex-

hibit shear banding and turbidity [HL04,LNWP]. The shear banding behavior and increasing turbidity occur in the intermediate shear-rate region when the stress plateaus. In the rectilinear shear situation, shear banding does occur for this model, albeit in a very small interval of shear-rates. The shear banding behavior is characterized by a velocity profile that quickly falls from the wall value through a boundary layer, then levels off, then falls rapidly again through an internal shear layer to a lower velocity through the middle of the gap, before rising symmetrically on the other side. For the rectilinear shear case no number density layers were seen for this model other than the depletion layers at the wall [CR04]. This situation may be considerably different in the case of a torsional shear flow such as a cone-plate or Taylor-Couette flow, due to the effects of spatial curvature. Experiments definitely suggest [SCMM03,LNWP,HL04] that shear layers first form near the inner wall where the curvature is highest.

In this paper, we examine the non-affine model developed in the previous paper, but in a circular Taylor-Couette flow. We compare the predictions with those available from experiments on micellar solutions [HL04,LFHY05,LNWP,SCMM03]. The geometry we study consists of two concentric cylinders with an inner cylinder of radius R_1, an outer cylinder of radius R_2 and a gap width of $H = R_2 - R_1$. The inner cylinder is held fixed while the outer cylinder rotates at velocity v. We consider both shear-rate controlled experiments(in which the velocity of the outer cylinder is prescribed) and stress controlled behaviors in steady state. Calculations show the formation of shear banding structures manifested both as sudden changes in the velocity gradient and as number density fluctuations. Results from the model are compared with experimental results for a micellar solution (surfactant system of 6% cetylpyridium chloride and 1.4% sodium salicylate (2:1 molar ratio) dissolved in .5M NaCl brine [HL04]). Additionally linear stability of the computed steady state solutions is examined.

2 Model

The physical variables involved in the analysis are denoted with a $\tilde{()}$ and are non-dimensionalized as follows: $r = \frac{\tilde{r}}{H}, t = \frac{\tilde{t}}{\lambda}, \mathbf{v} = \frac{\lambda \tilde{\mathbf{v}}}{H}, \boldsymbol{\tau} = \frac{\tilde{\boldsymbol{\tau}}}{n_{\rm av} kT}, n = \frac{\tilde{n}}{n_{\rm av}}$ where H is the gap width, k is the Boltzmann constant, T is temperature, and $n_{\rm av}$ is the average number density of micelles $n_{\rm av} = \int_{R_1}^{R_2} \tilde{r}\tilde{n}(\tilde{r})d\tilde{r}$.

Note that the typical velocity scale is based on the gap width and relaxation time, $v = \frac{H}{\lambda}$. This nondimensionalization results in two nondimensional parameters; namely the Deborah number $De = \frac{\lambda v}{H}$, the ratio of the relaxation time λ to the typical fluid flow time, and the Peclet number $\frac{Hv}{D_{tr}}$ where D_{tr} is the translational diffusivity of the micelles. With this scaling both shear-

rate controlled and stress-controlled cases can be examined easily through changes in boundary conditions only. The ratio of De to Pe, $\epsilon = \frac{De}{Pe} = \frac{\lambda D_{tr}}{H^2}$, is typically small [BAB91]. The parameter $\xi = 1 - a$ measures the extent of nonaffineness in the model, $\beta = \frac{\eta_s}{\eta_p}$ measures the solvent viscosity relative to the average "polymer" (micellar contribution to the) viscosity, $\eta_p = n_{ave} kT\lambda$. The Reynolds number for the flow is typically small, hence only inertialess flows are considered. Notation conventions are as in [BCAH87].

The dimensionless governing equations for the fluid flow are as follows. Conservation of mass:

$$\nabla \cdot \mathbf{v} = \mathbf{0}. \tag{1}$$

Conservation of momentum (inertialess flow):

$$\nabla \cdot \Pi = 0 \tag{2}$$

where

$$\Pi = p\boldsymbol{\delta} - \beta\dot{\boldsymbol{\gamma}} + \boldsymbol{\tau}_p \tag{3}$$

is the total stress. Here $\dot{\boldsymbol{\gamma}} = \nabla\mathbf{v} + (\nabla\mathbf{v})^t$. The dimensionless number density n and deviatoric stress $\boldsymbol{\tau}_p$ are given by,

$$a\frac{Dn}{Dt} = \epsilon\left(a\nabla^2 n + \nabla\nabla : \boldsymbol{\tau}_p + \xi\nabla\nabla : ((\boldsymbol{\tau}_p - an\boldsymbol{\delta})\cdot\dot{\boldsymbol{\gamma}})\right), \tag{4a}$$

$$\boldsymbol{\tau}_p + \boldsymbol{\tau}_{p(\diamondsuit)} - \epsilon\nabla^2\boldsymbol{\tau}_p - \left(a\frac{Dn}{Dt} - \epsilon a\nabla^2 n\right)\boldsymbol{\delta} = -a^2 n\dot{\boldsymbol{\gamma}}. \tag{4b}$$

Here $()_{(\diamondsuit)}$ represents the Gordon-Schowalter derivative:

$$()_{(\diamondsuit)} = \frac{D()}{Dt} - (\nabla_v)^t\cdot() - ()\cdot\nabla\mathbf{v} + \xi/2(\dot{\boldsymbol{\gamma}}\cdot\boldsymbol{\tau}_p + \boldsymbol{\tau}_p\cdot\dot{\boldsymbol{\gamma}}), \tag{5}$$

and

$$\boldsymbol{\tau}_p = an\boldsymbol{\delta} - \frac{aH_s}{n_{av}kT}\{\mathbf{QQ}\}, \tag{6}$$

where H_s is the Hookean spring force, $\mathbf{Q}$ is the connector vector between the two beads (from bead 1 to bead 2) in the bead-spring, and $\{\}$ signifies the ensemble average distribution. That is $\{\boldsymbol{QQ}\} = \sum_\nu \int \boldsymbol{QQ}\Psi_p d\boldsymbol{Q}$ where $\Psi_p(\tilde{r} - (-1)^\nu\boldsymbol{Q}/2, \boldsymbol{Q}, t)$ and $n = \Sigma_\nu \int \Psi d\boldsymbol{Q}$, (see [BAB91] [CR04]) where the sum is over the two beads $\nu = 1, 2$. Note that in the previous paper higher than second order moments were ignored in the closure. With a naive closure of the form $\{\boldsymbol{QQQQ}\} = \{\boldsymbol{QQ}\}\{\boldsymbol{QQ}\}/n$, it can be shown that these $O(\epsilon)$ terms are zero in steady shearing flow. Alternative closures are presently being investigated for their effect.

The boundary conditions for the problem are as in [CR04,BAB91]:

(1) No flux of micelles through the boundaries.

$$\hat{\mathbf{n}} \cdot \mathbf{j}_p = \hat{\mathbf{n}} \cdot a\nabla n + \nabla \cdot \boldsymbol{\tau}_p + \xi \nabla \cdot [(\boldsymbol{\tau}_p - an\boldsymbol{\delta}) \cdot \dot{\boldsymbol{\gamma}}] = 0 \tag{7}$$

(2) Conservation of the total number of micelles.

$$\int_\Omega \int n dA = 1 \tag{8}$$

(3) Alignment of the molecules at the wall.

$$\boldsymbol{\tau}_{pw} = an_w \left(\boldsymbol{\delta} - \frac{H_s \{Q^2\}_w}{kT\tilde{n}_w} (\hat{\mathbf{t}}\hat{\mathbf{t}}) \right) \tag{9}$$

(Here $\tilde{n}_w = n_{\text{av}} n_w$ is the dimensional number density at the wall, and $\hat{\mathbf{t}}$ is a unit tangent to the wall. Since flows considered in this paper will have no z dependence, $\hat{\mathbf{t}}$ is the tangent vector in the flow direction. Future work will examine three dimensional effects and thus will examine the effect of alignment of the micelles along the wall, but not necessarily solely in the flow direction. Further discussion of this boundary condition is given below.)

(4) Specification of either the velocity v (shear-rate controlled) or the stress $\boldsymbol{\tau} \cdot \hat{\boldsymbol{t}}$ (stress controlled) at the solid walls.

In this paper, we focus on the computation of steady solutions and their stability. Future work will examine time evolution of the flows from rest, dependence on initial state, and effects of different boundary conditions at the wall.

3 Axisymmetric Taylor-Couette Flow

We consider axisymmetric solutions to the system (1)-(19) for which the velocity has the form $u_r = 0, u_\theta = v(r), u_z = 0$. Here the subscripts indicate the component, and no variations in the θ or z directions are considered. Mass is automatically conserved and the components of the momentum equation (2) reduce to

$$\frac{1}{r^2} \frac{\partial}{\partial r} \left(r^2 \left[\tau_{pr\theta} - \beta r \frac{\partial}{\partial r} \left(\frac{v}{r} \right) \right] \right) = 0, \tag{10a}$$

(where $\beta = \eta_s/\eta_p$ as defined earlier)

$$\frac{1}{r} \frac{\partial}{\partial r} \left(r\tau_{prr} \right) - \frac{\tau_{p\theta\theta}}{r} + \frac{\partial p}{\partial r} = 0 \tag{10b}$$

The equations for the number density (4a) and extra stress components (4b) reduce to;

$$a\frac{\partial}{\partial t}n - \epsilon\left(a\frac{1}{r}\frac{\partial}{\partial r}\left(r\frac{\partial n}{\partial r}\right) + \frac{1}{r}\frac{\partial^2}{\partial r^2}(r\tau_{prr}) - \frac{1}{r}\frac{\partial}{\partial r}\tau_{p\theta\theta} + \xi\left[\frac{1}{r}\frac{\partial}{\partial r}\left\{r\frac{\partial}{\partial r}\left[\tau_{pr\theta}\left(r\frac{\partial}{\partial r}\left(\frac{v}{r}\right)\right)\right]\right\}\right]\right) = 0 \quad (10c)$$

$$\frac{\partial}{\partial t}\tau_{p\theta\theta} + \tau_{p\theta\theta} - 2\tau_{pr\theta}r\frac{\partial}{\partial r}\left(\frac{v}{r}\right) + \xi\tau_{pr\theta}r\frac{\partial}{\partial r}\left(\frac{v}{r}\right) - \epsilon\left[\frac{1}{r}\frac{\partial}{\partial r}\left(r\frac{\partial}{\partial r}\tau_{p\theta\theta}\right) + \frac{2}{r}\left(\tau_{prr} - \tau_{p\theta\theta}\right)\right] - \epsilon\left(\frac{1}{r}\frac{\partial^2}{\partial r^2}(r\tau_{prr}) - \frac{1}{r}\frac{\partial}{\partial r}\tau_{p\theta\theta} + \xi\left[\frac{1}{r}\frac{\partial}{\partial r}\left\{r\frac{\partial}{\partial r}\left[\tau_{pr\theta}\left(r\frac{\partial}{\partial r}\left(\frac{v}{r}\right)\right)\right]\right\}\right]\right) = 0 \quad (10d)$$

and

$$\frac{\partial}{\partial t}\tau_{pr\theta} + \tau_{pr\theta} - \tau_{prr}r\frac{\partial}{\partial r}\left(\frac{v}{r}\right) + \frac{\xi}{2}r\frac{\partial}{\partial r}\left(\frac{v}{r}\right)\left(\tau_{prr} + \tau_{p\theta\theta}\right) - \epsilon\left(\frac{1}{r}\frac{\partial}{\partial r}\left(r\frac{\partial}{\partial r}\tau_{pr\theta}\right) - \frac{4}{r}\tau_{pr\theta}\right) = -a^2nr\frac{\partial}{\partial r}\left(\frac{v}{r}\right) \quad (10e)$$

$$\frac{\partial}{\partial t}\tau_{prr} + \tau_{prr} + \xi r\frac{\partial}{\partial r}\left(\frac{v}{r}\right)\tau_{pr\theta} - \epsilon\left(\frac{1}{r}\frac{\partial}{\partial r}r\frac{\partial}{\partial r}\tau_{prr} - \frac{2}{r}\left(\tau_{prr} - \tau_{p\theta\theta}\right)\right) - \epsilon(\frac{1}{r}\frac{\partial^2}{\partial r^2}(r\tau_{prr}) - \frac{1}{r}\frac{\partial}{\partial r}\tau_{p\theta\theta} + \xi\left[\frac{1}{r}\frac{\partial}{\partial r}\left\{r\frac{\partial}{\partial r}\left[\tau_{pr\theta}\left(r\frac{\partial}{\partial r}\left(\frac{v}{r}\right)\right)\right]\right\}\right]) = 0 \quad (10f)$$

The boundary conditions at the walls ($r = r_1 = \frac{R_1}{H}, r = r_2 = \frac{R_2}{H}$) are that there is no flux.

$$a\frac{\partial n}{\partial r} + \frac{1}{r}\frac{\partial}{\partial r}\left(r\tau_{prr}\right) - \frac{\tau_{p\theta\theta}}{r} + \xi\left\{\frac{\partial}{\partial r}\left(\tau_{r\theta}r\frac{\partial}{\partial r}\left(\frac{v}{r}\right)\right)\right\} = 0,$$

and we specify the stress components:

$$\begin{aligned}
\tau_{prr}\Big|_w &= an_w, \\
\tau_{pr\theta}\Big|_w &= 0, \\
\tau_{p\theta\theta}\Big|_w &= an_w\left\{1 - \frac{H_s}{kT}\frac{\{\mathbf{QQ}\}_{\theta\theta}\Big|_w}{\tilde{n}_w}\right\} = an_w(1-d),
\end{aligned} \quad (11)$$

where $\boldsymbol{d}$ is the dimensionless second moment at the wall scaled with $\tilde{n}_w$ and the characteristic molecular length $\sqrt{k\tau/H_s}$ and either shear-rate controlled boundaries in which the velocity $v|_w$ is specified at both walls, or stress-controlled boundary conditions ($v = 0$ specified at one wall and stress specified on the other). Here $\tilde{n}_w = n_w n_{\rm av}$ is the dimensional value of the number density at the wall. Finally, the dimensionless number density must be conserved: $\int_{r_1}^{r_2} rn\, dr = 1$.

The problem outlined above is a singular perturbation problem in ϵ. For this problem ϵ is small. If $\epsilon = 0$ then there are no spatial derivatives of the stress left in the model, and the stress boundary conditions can not be satisfied. One expects, therefore, that the solution consists of pieces of an "outer" solution joined by boundary layers in which the solution variables (including the velocity field and number density) vary rapidly. In the "outer" regions the stress derivatives are order 1, in the boundary/shear layers the stress derivatives are order $\frac{1}{\epsilon^{1/2}}$. The lowest order outer stress for $\epsilon = 0$ is the solution to the Johnson-Segalman equation:

$$\tau_{pr\theta}^{(0)} = \frac{-a^2\dot{\gamma}^{(0)}}{1 + (1-a^2)(\dot{\gamma}^{(0)})^2}\ , \tag{12}$$

$$N_1^{(0)} = \tau_{prr}^{(0)} - \tau_{p\theta\theta}^{(0)} = \frac{2a^2(\dot{\gamma}^{(0)})^2}{1 + (1-a^2)(\dot{\gamma}^{(0)})^2}\ , \tag{13}$$

and also $n^{(0)} = 1$. Here $\dot{\gamma}^{(0)} = r(\frac{v_0}{r})'$ is one of the roots of (12). Note that the nondimensional value of shear rate $\dot{\gamma}^{(0)}$ is related to the dimensional value as in Section 2,

$$\dot{\gamma}^{(0)} = \frac{\tilde{r}\lambda\frac{\partial}{\partial\tilde{r}}\,(\tilde{v}/\tilde{r})}{H^2} = \lambda\tilde{\dot{\gamma}}^{(0)}. \tag{14}$$

The determination of which root should be selected can be made through matching with the shear/boundary layers. Notice that for a fixed value of a, $N_1^{(0)}$ increases with $\dot{\gamma}^{(0)}$ up to a maximum plateau value of $\frac{2a^2}{1-a^2}$ for $a < 1$. Thus the maximum value of the first normal stress difference increases as a gets closer to 1. If a is identically 1 then the shear stress is monotone as a function of shear rate, and $N_1^{(0)}$ increases, as $(\dot{\gamma}^{(0)})^2$, without bound.

4 Calculations and results

We calculate steady solutions to the system of equations (10) to explore general flow characteristics for comparison with similar laboratory experiments, and we also calculate the steady flow curve to confirm the existence of a plateau in the stress/shear-rate relationship. The non-dimensional geometric and parameter values are shown in Table 1. The non-dimensionalized geometry of our flow calculations are similar to the geometries of [HL04,SCMM03,LNWP]. The

value of ϵ was suggested by Rothstein [Rot03]. The results are presented in terms of the dimensionless gap variable $y = \frac{\tilde{r}-R_1}{H}$. The ratio of viscosities, β is the same as that used in [BAB91]. Most calculations were carried out with $a = 0.8$. However, we present results for $a = 0.9$ and $a = 1$ where necessary to show parameter sensitivities. Note that for $a = 1$ the motion is affine. The alignment of the micelles at the walls follows the choice of [BAB91] and the analysis of [MB92]. In fact in [MB92] the conformation tensor $\boldsymbol{C}$ is decomposed as $\boldsymbol{C} = n\boldsymbol{c}$ where $\boldsymbol{c}$ is a single molecule or specific configuration tensor. Mavrantzas and Beris found that not only does $\boldsymbol{c}$ align parallel to the wall, but that also $n_w = 0$. In our formalism n is allowed to adjust itself at the wall. The choice of d, that is the scaled second moment at the wall, needs more investigation. As will be seen, in the range $0 \leq d \leq 1$ the model predictions are relatively insensitive to d. Note that for this model, the quantity $\{\boldsymbol{QQ}\}$ is a weighted ensemble average of the molecular length which intrinsically involves the number density.

Parameter	R_1	Δ	v_1	v_2	ϵ	ξ or $1-a$	d	β
Value	15	1	0	De	10^{-3}	0.2	1/8	2.41×10^{-2}

Table 1
Flow geometry and fluid solution parameters for the calculations presented in this paper. All values are dimensionless.

The numerical techniques used for these calculations are very similar to those used in [CR04,KS01,SKR00]. We solve the boundary value problem with either shear-rate or stress controlled boundary conditions using fourth order spatial collocation where the number density at the inner cylinder wall, $n(R_1)$, is specified. To impose the number density constraint, we apply secant iterations using $n(R_1)$ as the independent variable. "Adams family" continuation methods are used to calculate solutions along the flow curve $\tau_{r\theta}(\dot{\gamma})$. The choice of shear-rate controlled or stress-controlled boundary conditions is not important except where the flow curve is close to horizontal (vertical) at which time it is necessary to use shear-rate (stress) controlled boundary conditions to continue solutions along the flow curve. For instance, when the flow curve is close to horizontal, the solution is very sensitive to stress-controlled boundary conditions, but one can converge rapidly to a solution by specifying the shear rate.

To construct the flow curve, we calculate steady solutions for a typical Couette cell geometry and typical flow parameters as shown in Table 1. In Figure 1, we see that the new model produces a flow curve with a distinct plateau. The

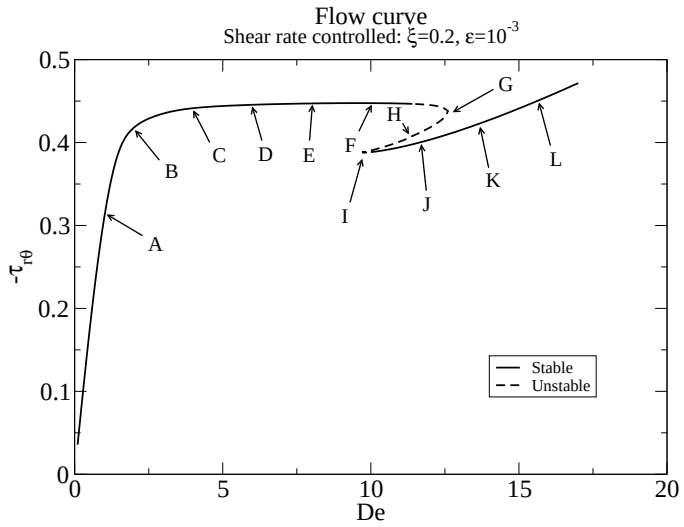

Fig. 1. A flow curve using parameters provided in Table 1. The total stress is measured at the outer wall.

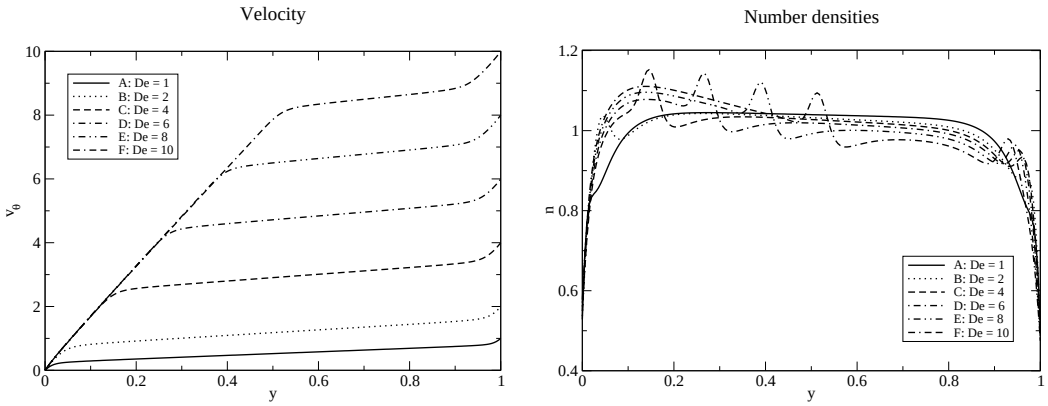

(a) (b)

Fig. 2. Flow velocity and number densities along the left stable branch of the flow curve at positions A-F.

vertical axis represents the total shear stress,

$$\tau_{r\theta} = \tau_{pr\theta} - \beta r \left(\frac{v}{r}\right)',$$

measured at the outer wall $r = R_2$. (Hereafter $()'$ represents $\frac{d}{dr}$ or $\frac{\partial}{\partial r}$ as the case may be). The horizontal axis is the dimensionless apparent shear rate $De = \lambda v/H$. As we see in Figure 2, the local velocity gradient of $\frac{\partial v_\theta}{\partial y}$ is not uniform across the gap. Hence, we plot the spatial variations in the velocity profile for various apparent shear rates. The homogeneous solution corresponds to a linear velocity profile $v_\theta = Dey$. Along the flow curve, as we increase the Deborah number up to the plateau values of stress, a boundary layer in the flow velocity forms at the inner cylinder. The velocity in the boundary layer at the

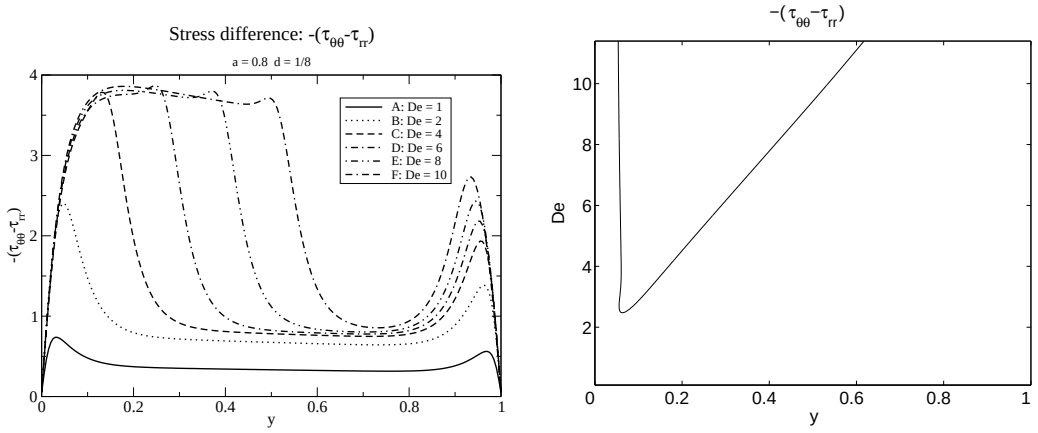

(a) (b)

Fig. 3. In (a), radial variations in the first normal stress difference are plotted against the apparent shear rate. At right, (b) we show the spatial extent of first normal stress difference contour for $N_1 = 3$ as Deborah number is increased

inner cylinder develops a linear profile, and grows into the gap as the apparent shear rate increases. As De is increased from 2.5 to 10, the total stress remains constant, that is the flow curve corresponding to the imposed stress/strain-rate has a plateau. The width of the high shear rate band, starting from the inner cylinder, grows as the apparent shear rate increases. A modest boundary layer also forms at the outer cylinder to attain the correct outer cylinder velocity. The computed velocity profile shows a two banded structure with one sharp transition region (and a third boundary layer near the outer wall Figure 2a, the width of which goes to zero as ϵ goes to zero) similar to those profiles measured by Hu and Lips [HL04], Liberatore et al, [LNWP] and Salmon et al, [SCMM03] in Couette geometries, although the latter profiles do not exhibit the boundary layer at the outer cylinder. In the latter two cases, the outer cylinder remains stationary whilst the inner rotates.

As observed in our study of rectilinear flow there is a depletion in the local concentration of micelles near the wall. However, in this cylindrical geometry, two distinct local maxima or number density bands form, one near the inner and one near the outer cylinder walls. In Figure 2, we see that the inner aggregation layer of micelles moves into the gap as the shear-rate increases. The much smaller local maxima near the outer wall remains roughly unchanged as the shear-rate grows and this is a consequence solely of the no flux/no penetration boundary condition. By contrast, the notable local maximum in concentration toward the inner wall occurs in the region where the velocity gradient changes sharply. This local change in fluid density may well be connected to the onset of turbidity that is observed experimentally. [BRP94]

To understand the alignment and stretching of the molecules, we examine the

first normal stress difference,

$$N_1 = -(\tau_{p\theta\theta} - \tau_{prr}) = \frac{aH_s}{n_{\rm av}kT}\left(\{\mathbf{QQ}\}_{\theta\theta} - \{\mathbf{QQ}\}_{rr}\right). \tag{15}$$

At the wall, the stress difference is specified to be,

$$N_1 = -\left(\tau_{p\theta\theta} - \tau_{prr}\right)|_w = \frac{aH_s}{n_{\rm av}kT}\{\mathbf{QQ}\}_{\theta\theta} = an_w d. \tag{16}$$

In Figure 3, we see that a region with strong molecular alignment or stretching originates near the inner cylinder and grows into the gap as the apparent shear rate grows. This alignment reaches a maximum value for large enough shear rates, $De \gtrsim 4$, and the maximum is subsequently independent of De. The value of this maximum depends only on a as predicted by the outer solution (13) for large $\dot{\gamma}^{(0)}$ and as discussed in the next paragraph. The sharp downward transition in the first normal stress difference that signifies the end of the aligned/stretched region is associated with the local maximum in number density (see Figure 2 for comparison). In experiments, the shear-induced phase transitions that develop as the shear rate is steadily increased are associated with strong local stretching and concomitant increases in the turbidity or local number density [LGHCP04] that are reminiscent of those predicted by the present model. Figure 3 (a) shows the growth of the alignment/stretched region across the gap. Figure 3 (b) follows the steady propagation of the $N_1 = 3$ contour across the gap as the De number increases. Although we have chosen this contour arbitrarily this criterion may represent, at least qualitatively, a suitable condition for the onset of a shear-induced structural transition beyond a critical degree of stretching that results in sample turbidity. Note that this high-stress turbidity-prone region is not at the wall, but is located close to the inner surface and expands into the gap as the shear rate increases. This is also consistent with birefringence experiments [LFHY05,LNK$^+$].

Continuing along the flow curve past the plateau, the right hand (stable) branch exhibits solutions with flow profiles that are close to Newtonian, and the number density distribution remains unchanged with increasing De (as shown in Figure 4).

To examine the sensitivity of the first normal stress difference to variations in constitutive parameters, we varied the parameters a and d. Calculations show that there are no changes in the first normal stress difference across the gap as d is varied between 0 and 1. The model predictions are insensitive to variations in d in this range. Note from (11) the boundary conditions assume that the micelles are aligned at the wall ($\{\mathbf{QQ}\}_{rr} = 0$) and d measures the scaled extension of the micelles along the wall. The results are thus insensitive to this parameter at least in the range $0 \leq d \lesssim 1$. Figure 5 shows a comparison of the first normal stress difference with variations in a. It is particularly interesting to note the extreme sensitivity of the model to changes in a. When

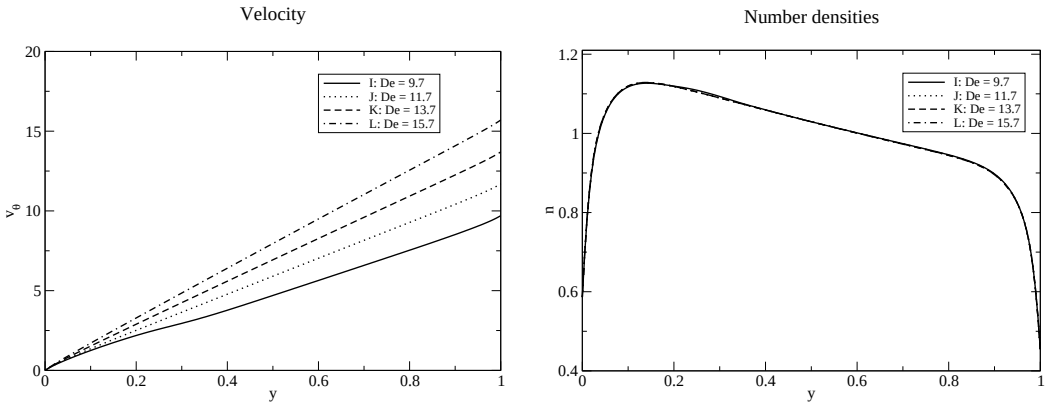

(a) (b)

Fig. 4. Flow velocity and number densities along the right stable branch of the flow curve at positions I-L. The number density curves superpose one another.

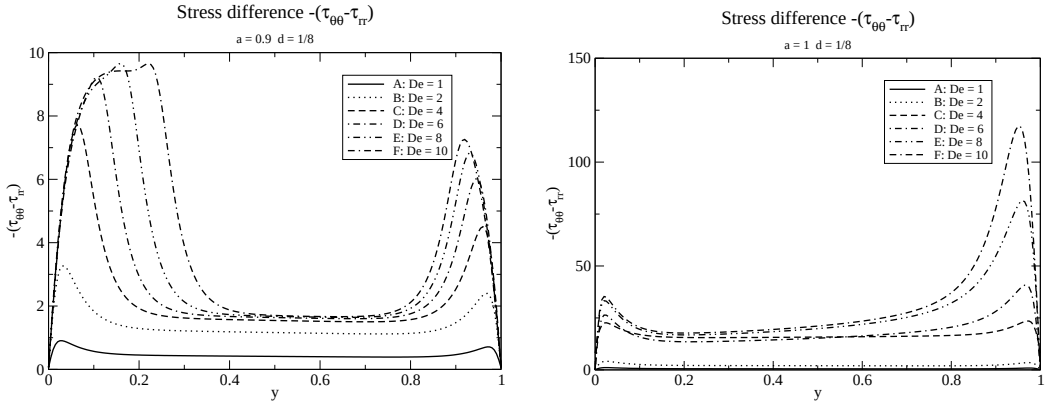

(a) (b)

Fig. 5. First normal stress difference for $a = 0.9$ (a) and $a = 1$ (b). These should be compared with Figure 3 (a) where $a = 0.8$.

$a = 1$ the underlying flow curve is monotone and the model reduces to the (corrected) Bhave, Armstrong, Brown model. The first normal stress difference has a large maximum near, but not at, the outer wall for $a = 1$. As a decreases, a maximum in N_1 develops near, but not at, the inner wall, and the location at which this maximum is obtained propagates into the gap as De increases. As a decreases the magnitude of this maximum decreases, but the growth of the region of maximum first normal stress propagates more quickly into the interior. Since calculations show that the radial variation in the number density $n(r)$ does not vary appreciably with a, (certainly not as strongly as N_1), the increase of the first normal stress is primarily due to an increase in either the number of molecules aligned in the flow direction and/or the length of these molecules. Note that the plateau values of N_1 agree with those

predicted for large $\dot{\gamma}$ which are also the maximum and the asymptote for the zeroth order solution (12), namely $\frac{2a^2}{(1-a^2)}$. Note that this value, the asymptote of the zeroth order solution and the maximum observed in the full numerical calculations is independent of $\dot{\gamma}$.

5 Stability

To calculate the linear stability of the steady solutions that are obtained along the flow curve, we consider the growth or decay of small perturbations to steady solutions.

$$n(r,t) = \bar{n}(r) + \delta\tilde{n}(r)e^{\lambda t} \tag{17a}$$
$$\tau_{prr}(r,t) = \bar{\tau}_{prr}(r) + \delta\tilde{\tau}_{prr}(r)e^{\lambda t} \tag{17b}$$
$$\tau_{p\theta\theta}(r,t) = \bar{\tau}_{p\theta\theta}(r) + \delta\tilde{\tau}_{p\theta\theta}(r)e^{\lambda t} \tag{17c}$$
$$\tau_{pr\theta}(r,t) = \bar{\tau}_{pr\theta}(r) + \delta\tilde{\tau}_{pr\theta}(r)e^{\lambda t} \tag{17d}$$
$$v(r,t) = \bar{v}(r) + \delta\tilde{v}(r)e^{\lambda t} \tag{17e}$$

where $\delta \ll 1$ and λ is complex. Substituting (17) into (10) and collecting all terms at order δ, we obtain the following eigenvalue/eigenfunction problem.

$$\lambda\tilde{n} = \epsilon\left[\frac{1}{r}\left(r\tilde{n}'\right)' + \Xi/a\right] \tag{18a}$$
$$\begin{aligned}\lambda\tilde{\tau}_{prr} =& -\tilde{\tau}_{prr} - \xi\left[r\left(\frac{\bar{v}}{r}\right)'\tilde{\tau}_{pr\theta} + \bar{\tau}_{pr\theta}r\left(\frac{\tilde{v}}{r}\right)'\right] \\ &+ \epsilon\left[\frac{1}{r}\left(r\tilde{\tau}'_{prr}\right)' + \frac{2}{r}\left(\tilde{\tau}_{p\theta\theta} - \tilde{\tau}_{prr}\right) + \Xi\right]\end{aligned} \tag{18b}$$
$$\begin{aligned}\lambda\tilde{\tau}_{p\theta\theta} =& -\tilde{\tau}_{p\theta\theta} + (2-\xi)\left[r\left(\frac{\bar{v}}{r}\right)'\tilde{\tau}_{pr\theta} + \bar{\tau}_{pr\theta}r\left(\frac{\tilde{v}}{r}\right)'\right] \\ &+ \epsilon\left[\frac{1}{r}\left(r\tilde{\tau}'_{p\theta\theta}\right)' + \frac{2}{r}\left(\tilde{\tau}_{prr} - \tilde{\tau}_{p\theta\theta}\right) + \Xi\right]\end{aligned} \tag{18c}$$
$$\begin{aligned}\lambda\tilde{\tau}_{pr\theta} =& -\tilde{\tau}_{pr\theta} + \left[\bar{\tau}_{prr} - \frac{\xi}{2}\left(\bar{\tau}_{prr} + \bar{\tau}_{p\theta\theta}\right)\right]r\left(\frac{\tilde{v}}{r}\right)' \\ &+ \left(1 - \frac{\xi}{2}\right)r\left(\frac{\bar{v}}{r}\right)'\tilde{\tau}_{prr} - \frac{\xi}{2}r\left(\frac{\bar{v}}{r}\right)'\tilde{\tau}_{p\theta\theta} \\ &+ \epsilon\left[\frac{1}{r}\left(r\tilde{\tau}'_{pr\theta}\right)' - \frac{4}{r}\tilde{\tau}_{pr\theta}\right] - a^2\left[\bar{n}r\left(\frac{\tilde{v}}{r}\right)' + r\left(\frac{\bar{v}}{r}\right)'\tilde{n}\right]\end{aligned} \tag{18d}$$
$$\lambda\mathrm{Re}\ \tilde{v} = -\frac{1}{r^2}\left\{r^2\left[\tilde{\tau}_{pr\theta} - \beta r\left(\frac{\tilde{v}}{r}\right)'\right]\right\}' \tag{18e}$$

where

$$\Xi = \frac{1}{r}\left((r\tilde{\tau}_{prr})'' - \tilde{\tau}'_{p\theta\theta} + \xi\left\{r\left[r\left(\frac{\bar{v}}{r}\right)'\tilde{\tau}_{pr\theta} + \bar{\tau}_{pr\theta}r\left(\frac{\tilde{v}}{r}\right)'\right]\right\}'\right) \tag{18f}$$

For the last condition, it is understood that $\mathrm{Re} \ll 1$, and this condition is automatically satisfied because one can perturb (10a) and apply the perturbation boundary conditions to find that

$$\tilde{\tau}_{pr\theta} - \beta r\left(\frac{\tilde{v}}{r}\right)' = -\beta v'(R_1)\frac{R_1^2}{r^2}. \tag{19}$$

The boundary conditions for the perturbed equations are

$$\left\{a\tilde{n}' + \frac{1}{r}\left(r\tilde{\tau}'_{prr}\right)' - \frac{1}{r}\tilde{\tau}_{p\theta\theta} + \xi\left[r\left(\frac{\bar{v}}{r}\right)'\tilde{\tau}_{pr\theta} + \bar{\tau}_{pr\theta}r\left(\frac{\tilde{v}}{r}\right)'\right]'\right\}\Big|_w = 0 \tag{20a}$$

$$(\tilde{\tau}_{prr} - a\tilde{n})\big|_w = 0 \tag{20b}$$

$$[\tilde{\tau}_{p\theta\theta} - a(1-d)\tilde{n}]\big|_w = 0 \tag{20c}$$

$$\tilde{\tau}_{pr\theta}\big|_w = 0 \tag{20d}$$

$$\tilde{v}(R_1) = 0 \tag{20e}$$

$$\tilde{v}(R_2) = 0 \quad \text{(strain rate controlled)} \tag{20f}$$

$$r\left(\frac{\tilde{v}}{r}\right)'\Big|_{r=R_2} = 0 \quad \text{(stress controlled)} \tag{20g}$$

For stress-controlled computations, we find a rich bifurcation structure along the plateau, and we leave the exploration of these bifurcations for future investigation. We will focus our attention on strain rate controlled boundary conditions for the remainder of this paper.

The evolution of the spectrum of the perturbed system (18) between F and G along the plateau, and near I at the cusp when moving from J toward H, characterizes the transitions to instability. Figure 6 shows that in the transition from F to G, a single pair of complex conjugate eigenvalues cross into the right half-plane, indicating a spiral node instability which is fundamentally different from model behavior for rectlinear shear flows [CR04]. This instability would be expected if the system were going through a Hopf bifurcation as indicated by experimental observations. In Figure 7 (a), we include the corresponding plot of the growing temporal oscillations in the number density, suggesting that fluctuations in n and optical properties such as turbidity would be observed in experiments. Figure 7 (b) shows the corresponding first normal stress difference. However, moving past the cusp from the righthand "Newtonian-like" branch of the flow curve near I moving toward H, we observe a standard saddle-node transition as shown in Figure 8. A plot of the

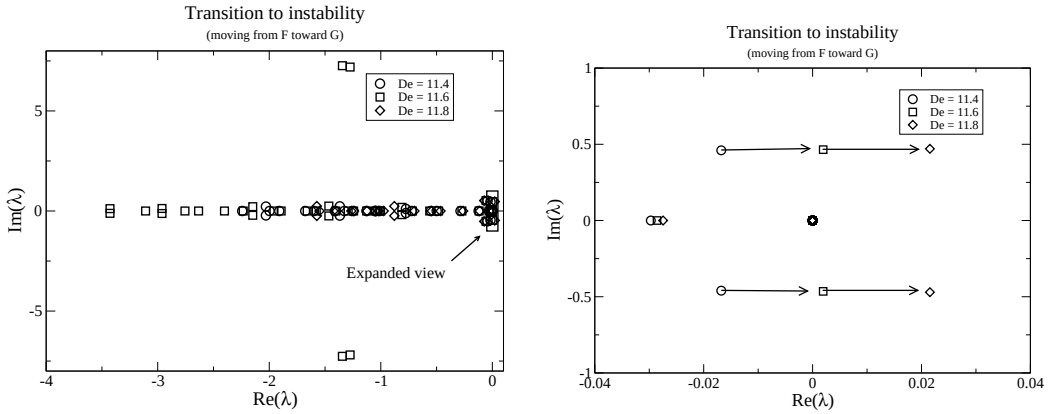

(a) (b)

Fig. 6. The transition to instability along the plateau. The transition from stable to unstable occurs between points F and G on the flow curve in Figure 1. Figure (a) shows the relevant portion of the numerical spectrum of the eigensystem described in (18) for three solutions that straddle the transition from stable to unstable. The first solution lies on the stable side of the transition and the latter two lie to the right of the transition point. Figure (b) is an expanded view of the spectrum at the origin and clearly indicates a spiral node instability. Neutrally stable translational modes located at the origin correspond to imposition of the zero perturbation number density constraint.

exponentially growing number density perturbation is shown in Figure 7 (c). Linear stability analysis does not reveal the direction or sign of the growing disturbance, but we can expect complimentary changes near the inner and outer walls as we move past the cusp at point I, corresponding to a jump to a point between E and F if one were decreasing De. Figure 7 (d) shows the analogous behavior for the perturbed first normal stress difference.

6 Conclusions

In this paper, we have examined a model for dilute wormlike micellar solutions with coupled stress and number density in axisymmetric Taylor-Couette flows. We have applied this model with parameters selected to characterize an experimental geometry that is similar to those of a number of investigators in their laboratory experiments. Calculations of the stress/strain-rate flow curve exhibit a pronounced plateau region similar to those measured in laboratory experiments. We find that coupling stress and number density provides a selection mechanism for regions in which the stress/strain-rate curve are multi-valued in agreement with our earlier results for rectilinear shear flows. However, the circular geometry reveals several notable differences. With the

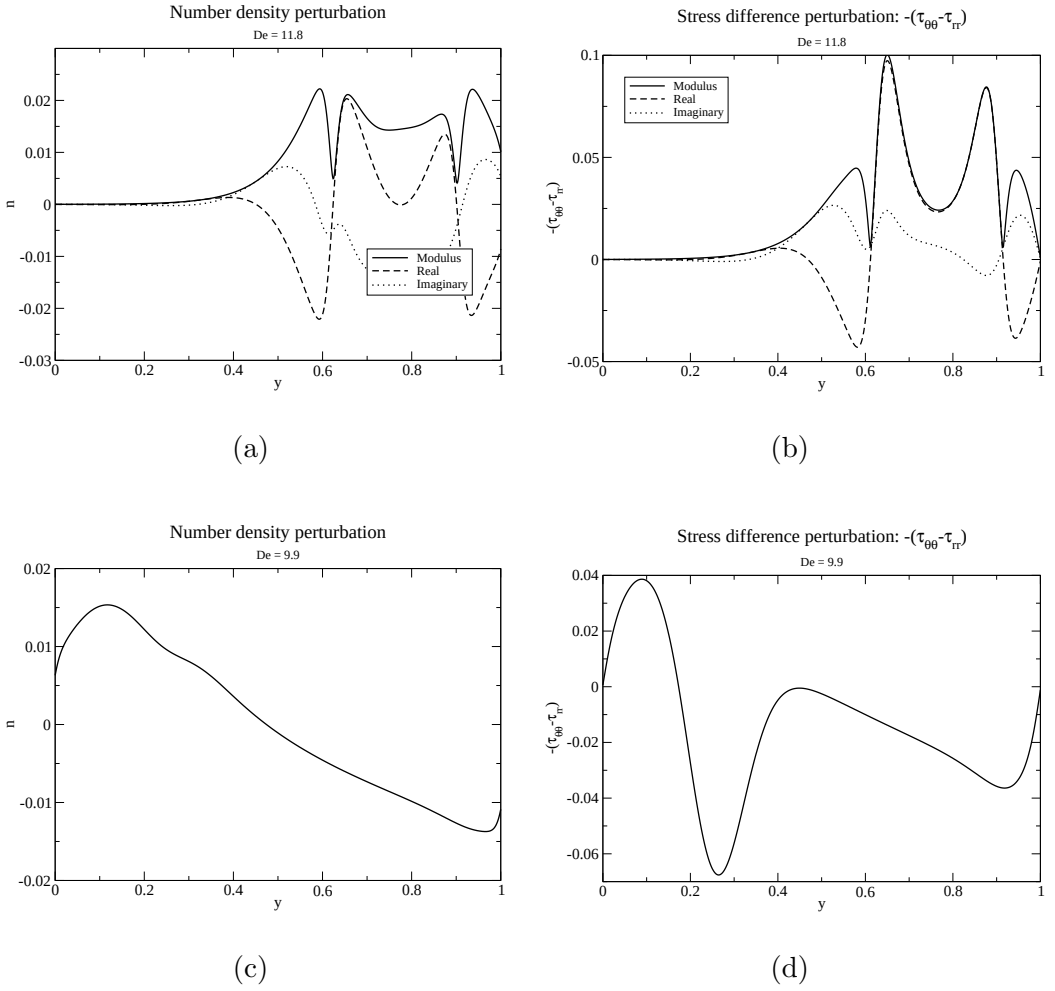

Fig. 7. Modes of instability. Plot (a) shows the real part, imaginary part and modulus of the number density perturbation corresponding to the unstable spiral node, and (b) shows the first normal stress difference perturbation. Similarly, plots (c) and (d) show the saddle node perturbation number density and first normal stress difference. (Since the eigenvalue is real, the eigenfunction is also real in the last two plots.)

curvilinear geometry, the shearbands that develop in the gap are no longer symmetric about each wall. Rather, the inner boundary layer grows with apparent shear rate until it is no longer a boundary layer but rather a full fledged shear rate band that extends over 50% of the gap. At the same time, the outer boundary layer experiences very little change. For the circular geometry, we find that the transition to instability along the plateau in the flow curve involves a complex conjugate pair of eigenvalues indicative of a spiral node instability whereas the instability mode for rectilinear shear flow involved a simple real eigenvalue indicative of a saddle node instability. Experimentally, this loss of stability would be observed as growing time dependent fluctuations in the local number density and optical anisotropy of the fluid in the middle of the gap of a Taylor-Couette cell. Similar observations have been

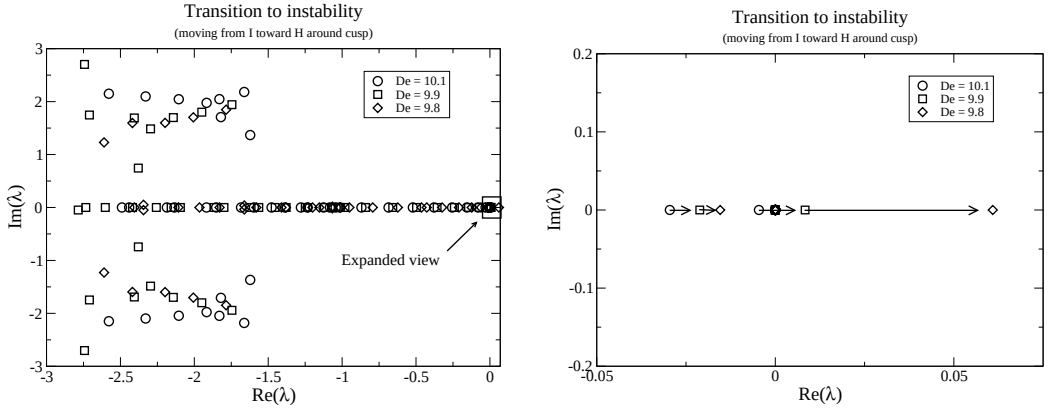

(a) (b)

Fig. 8. The transition to instability near the cusp. The transition from stable to unstable occurs between near I moving toward H on the flow curve in Figure 1 as one travels away from the right branch. Figure (a) shows the relevant portion of the numerical spectrum of the eigensystem described in (18) for three solutions that straddle the cusp. The first solution lies on the stable side of the transition and the latter two lie to the right of the transition point. Figure (b) is an expanded view of the spectrum at the origin and clearly indicates a saddle node instability. Again, neutrally stable translation modes located at the origin correspond to imposition of the zero perturbation number density constraint.

made experimentally [LFHY05,LGHCP04] . Finally, we see regions of strong molecular alignment or stretching that originate near the inner cylinder at low apparent strain rates and propagate into the gap as the apparent strain-rate increase in a manner similar to experimental observation. If a critical tensile stress difference can be associated with micellar rupture and onset of turbidity then the model also captures the progressive growth of turbid regions near the rotating inner cylinder as the imposed deformation rate is increased.

7 Acknowledgments

This work was supported by National Science Foundation grant DMS-0405931 and DMS-0406590.

References

[BAB91] A. V. Bhave, R. C. Armstrong, and R. A. Brown. Kinetic theory and rheology of dilute, non-homogeneous polymer solutions. *J. Chem. Phys.*, 95(14) August:pp. 2988–3000, 1991.

[BCAH87] R. B. Bird, C. F. Curtiss, R. C. Armstrong, and O. Hassager. *Dynamics of Polymeric Liquids: Vol 2, Kinetic Theory.* John Wiley and Sons, New York, second edition, 1987.

[Ber97] J.F. Berret. Transient rheology of wormlike micelles. *Langmuir*, 13(5):2227–2234, 1997.

[BM94] A. N. Beris and V. G. Mavrantzas. On the compatibility between various macroscopic formalisms for the concentration and flow of dilute polymer solutions. *J. Rheol.*, 38(5):1235–1250, Sept/Oct 1994.

[BRP94] J.F. Berret, D.C. Roux, and G. Porte. Isotropic-to-nematic transition in wormlike micelles under shear. *J. Phys.II (France)*, 4:1261–1279, 1994.

[Cat87] M. E. Cates. Reptation of living polymers: Dynamics of entangled polymers in the prescence of reversible chain-scission reactions. *Macromolecules*, 20:2289–2296, 1987.

[CR04] L. P. Cook and L. Rossi. Shear layers and demixing in a model for shear flow of self-assembling miceller solutions. *J. Non-Newt. Fluid Mech.*, 116:347–369, 2004.

[EYB96] P. Espanol, X.F. Yuan, and R.C. Ball. Shear banding flow in the Johnson-Segalman fluid. *Journal of non-Newtonian Fluid Mechanics*, 65:93–109, 1996.

[FO03a] S. M. Fielding and P. D. Olmsted. Early stage kinetics in a unified model of shear-induced demixing and mechanical shear banding instabilities. *Phys. Eev. Lett.*, 90:2240501–1–2240501–4, 2003.

[FO03b] S. M. Fielding and P. D. Olmsted. Kinetics of shear banding instability in startup flows. *Phys. Rev. E*, 68:036313–1–036313–2, 2003.

[FO04] S. M. Fielding and P. D. Olmsted. Spatiotemporal oscillations and rheochaos in a simple model of shear banding. *Phys. Rev. Lett.*, 9:084502–1–084502–4, 2004.

[GB97] F. Greco and R.C. Ball. Shear-band formation in a non-Newtonian fluid model with a constitutive instability. *J. Non-Newt Fluid Mech.*, 69:195–206, 1997.

[HL04] Y. T. Hu and A. Lips. Kinetics and mechanism of shear banding in entangled micellar solutions. 2004.

[KS01] J Kierzenka and L F Shampine. A BVP solver based on residual control and the Matlab PSE. *ACM Trans. Math. Software*, 27(3):299–316, 2001.

[Lar88] R. G. Larson. *Constitutive Equations for Polymer Melts and Solutions.* Butterworths, 1988.

[LFHY05] J.Y. Lee, G.G. Fuller, N.E. Hudson, and X.F. Yuan. Investigation of shear-banding structure in wormlike micellar solution by point-wise flow-induced birefringence measurements. *J. Rheology*, 49 (2):537–550, 2005.

[LGHCP04] M. R. López-Gonzáles, W. M. Holmes, P. T. Callahan, and P. J. Photinos. Shear banding fluctuations and nematic order in wormlike micelles. *Phys. Rev. Lett.*, 93:2268302–1–2268302–4, 2004.

[LNK$^+$] M. W. Liberature, F. Nettlesheim, E. W. Kaler, N. J. Wagner, T. Nu, and L.Porcar. Characterization of solutions of wormlike micelles underflow: Microstructure and investigations in the 1-2 plane (preprint).

[LNWP] M. W. Liberatore, F. Netlesheim, N. J. Wagner, and L. Porcar. Spatially resolved sans in the 1-2 plane: A study of shear-induced phase separating wormlike micelles (preprint).

[LOB00] C.-Y. David Lu, P. D. Olmsted, and R. Ball. Effects of nonlocal stress on the determination of shear banding flow. *Physical Review Letters*, 84(4):642–645, January 2000.

[MB92] V. G. Mavrantzas and A. N. Beris. Theoretical study of wall effects on rheology of dilute polymer solutions. *J. Rheo.*, 36(1):175–213, Jan 1992.

[NP97] J. A. Nohel and L. Pego. On the generation of discontinuous shearing motions of a non-newtonian fluid. *Arch Rational Mech. Anal.*, 139:pp. 355–376, 1997.

[Olm99] P. Olmsted. Dynamics and flow-induced phase separation in polymeric fluids. *Current opinion in colloid and interface science*, 4(2):95–100, April 1999.

[ORL00] P.D. Olmsted, O. Radulescu, and C.-Y.D. Lu. Johnson-Segalman model with a diffusion term in cylindrical Couette flow. *J. Rheol*, 44(2):257–275, March/April 2000.

[RH91] H. Rehage and H. Hoffmann. Viscoelastic surfactant solutions: Model systems for rheological research. *Molecular Physics*, 74(5):pp. 933–973, 1991.

[RO00] O. Radulescu and P. D. Olmsted. Matched asymptotic solutions for the steady banded flow of the diffusive Johnson-Segalman model in various geometries. *J of Non-Newt Fluid Mech.*, 91:143–164, 2000.

[Rot03] J. Rothstein. Personal conversation. 2003.

[SCMM03] J.B. Salmon, A. Colin, S. Manneville, and F. Molino. Velocity profiles in shear-banding wormlike micelles. *Phys. Rev. Letters*, 90 (22):228303–1 – 228303–4, (June 6) 2003.

[SKR00] L. F. Shampine, J. Kierzenka, and M. W. Reichelt. Solving boundary value problems for ordinary differential equations in Matlab with bvp4c. Technical report, The MathWorks, ftp://ftp.mathworks.com/pub/doc/papers/bvp/, 2000.

[WFF98] E. K. Wheeler, P. Fischer, and G G. Fuller. Time-periodic flow induced structures and instabilities in a viscoelastic surfactant solution. *J. Non-Newt Fluid Mech.*, 75:pp. 193–208, 1998.

[WHC03] M.R. López-González W.M. Holmes and P.T. Callaghan. Fluctuations in shear-banded flow seen by nmr velocimetry. *EuroPhysics Letter*, 64 (2):274–280, 2003.